RSC Advances

PAPER

View Article Online
View Journal | View Issue

Cite this: *RSC Adv.*, 2024, **14**, 7081

Br doping-induced evolution of the electronic band structure in dimorphic and hexagonal $SnSe_2$ thermoelectric materials†

Se-Jun Kim,‡[a] Minsu Heo,‡[a] Sang-il Kim,‡[a] Hyunjin Park,[a] Jeong-Yeon Kim,[a] Won-Seon Seo[b] and Hyun-Sik Kim*[a]

Received 13th November 2023
Accepted 11th February 2024

DOI: 10.1039/d3ra07751a

rsc.li/rsc-advances

$SnSe_2$ with its layered structure is a promising thermoelectric material with intrinsically low lattice thermal conductivity. However, its poor electronic transport properties have motivated extensive doping studies. Br doping effectively improves the power factor and converts the dimorphic $SnSe_2$ to a fully hexagonal structure. To understand the mechanisms underlying the power factor improvement of Br-doped $SnSe_2$, the electronic band parameters of Br-doped dimorphic and hexagonal $SnSe_2$ should be evaluated separately. Using the single parabolic band model, we estimate the intrinsic mobility and effective mass of the Br-doped dimorphic and hexagonal $SnSe_2$. While Br doping significantly improves the mobility of dimorphic $SnSe_2$ (with the dominant hexagonal phase), it results in a combination of band convergence and band flattening in fully hexagonal $SnSe_2$. Br-doped dimorphic $SnSe_2$ is predicted to exhibit higher thermoelectric performance (zT ~0.23 at 300 K) than Br-doped fully hexagonal $SnSe_2$ (zT ~0.19 at 300 K). Characterisation of the other, currently unidentified, structural phases of dimorphic $SnSe_2$ will enable us to tailor the thermoelectric properties of Br-doped $SnSe_2$.

Global warming is disrupting ecosystems and reducing biodiversity, which is threatening food production and human well-being.[1,2] The emission of greenhouse gases, such as carbon dioxide (CO_2), is a major cause of global warming. Fossil fuels, such as coal, oil, and natural gas, are the main source of CO_2 emissions. The burning of these fuels releases CO_2 into the atmosphere, where it traps heat and contributes to climate change.[3] Renewable and sustainable power generation technologies, such as solar, wind, and hydropower, offer a way to reduce CO_2 emissions and combat global warming. These technologies do not produce greenhouse gases, and they can be used to generate electricity, heat homes and businesses, and power transportation.[4] Among these renewable and sustainable power generation technologies, thermoelectric power generation technology is the only technology that can directly generate electricity from waste heat.[5] The efficiency of thermoelectric devices is a key factor in their ability to convert waste heat into electrical energy. The higher the efficiency, the more electrical energy can be produced from the same amount of waste heat.[6] To improve the efficiency of a thermoelectric power generation device, the performance of the thermoelectric materials used in the device should be increased. The thermoelectric performance of the material is defined with a dimensionless figure-of-merit, zT. The zT is expressed by the following eqn (1)

$$zT = \frac{S^2\sigma T}{\kappa_e + \kappa_l} \quad (1)$$

where S, σ, T, κ_e, and κ_l are the Seebeck coefficient, electrical conductivity, absolute temperature, electronic thermal conductivity, and the lattice thermal conductivity, respectively.[7–10] As evident from eqn (1), to achieve a high zT, it is essential to increase the power factor (PF), which is the product of the S and the σ, and simultaneously lower the κ_l (the κ_e is linked to the σ). Unfortunately, the S and σ are in a trade-off relationship. This means that it is difficult to improve both S and σ at the same time.[11] However, there are ways to increase the zT despite the coupled relationship between the S, σ, and κ_e. One strategy is to increase PF *via* band engineering (band convergence and resonant states formation), which overcomes the trade-off relationship between the S and σ.[12–15] Another strategy is to reduce κ_l that is independent of other parameters in zT *via* defect engineering.[16–18]

Among the various thermoelectric materials, $SnSe_2$ has received much attention because it has an intrinsically low κ_l due to its layered structure.[19] The layered structure has a distinct difference between the bonding forces within layers and between layers. The bonds within the layer are covalent bonds, which are strong chemical bonds. The bonds between

[a]*Department of Materials Science and Engineering, University of Seoul, Seoul 02504, South Korea. E-mail: hyunsik.kim@uos.ac.kr*

[b]*Department of Materials Science and Engineering, Yonsei University, Seoul 03722, South Korea*

† Electronic supplementary information (ESI) available. See DOI: https://doi.org/10.1039/d3ra07751a

‡ These authors contributed equally to this study.

layers are van der Waals bonds, which are weaker secondary bonds. As a result, the κ_l along the axis of van der Waals bonding is low, which contributes to lowering κ_l.[20–22] However, pristine $SnSe_2$ has a low PF due to low σ.[8] Wu *et al.* significantly increased Hall carrier concentration (n_H) and Hall mobility (μ_H) compared to the pristine $SnSe_2$ by Cl doping (12 mol%) at the Se sites. Consequently, the PF is significantly improved (0.0175 → 1.05 mW m^{-1} K^{-2}) compared to pristine $SnSe_2$ near room temperature.[23] Wang *et al.* fabricated Cu-doped $SnSe_2$, which resulted in a lower S compared to pristine $SnSe_2$, but a higher PF (1.96 mW m^{-1} K^{-2}) at 300 K due to an increase in n_H.[24] Li *et al.* achieved a high PF (0.35 mW m^{-1} K^{-2}) by doping Ag at the Sn sites (1 mol%). The PF increase owing to the Ag doping could be attributed to the S improvement that outweighed the σ decrease. Although Ag doping improved the μ_H, it decreased the n_H to an extent that the σ decreased with Ag doping.[25] Zhou *et al.* improved the PF (1.2 mW m^{-1} K^{-2}) of $SnSe_2$ by co-doping Cu (between the layers of $SnSe_2$) and Br (within the layers). The co-doping improved the σ by increasing the n_H and μ_H at the same time.[22] Recently, Liu *et al.* reported that Br doping at Se sites ($SnSe_{2-x}Br_x$ for $x = 0$, 0.01, 0.03, 0.05, and 0.10) was effective in improving the PF.[26] They confirmed that both the n_H and μ_H increased (hence the σ increased) as the Br doping content increased up to $x = 0.05$. $SnSe_2$ has a dimorphic structure, meaning that it can exist in two different crystal structures: hexagonal and unidentified structure.[29–31] These two structures can coexist stably. Liu *et al.*[26] found that the fraction of the hexagonal structure in $SnSe_2$ increased for the Br doping content (x) smaller than 0.05 (although the hexagonal structure is already dominant). However, only the hexagonal structure was detected for $x \geq 0.05$. In other words, the Br doping promoted the fraction of the hexagonal structure and increased the n_H for $x < 0.05$, while it only increased the n_H for $x \geq 0.05$. However, how the fraction of hexagonal structure increase (induced by the Br doping) and the Br doping (when $SnSe_2$ is fully hexagonal) affect the electronic band structure of $SnSe_2$ is not studied.

In this study, changes in the electronic band structure of $SnSe_2$ were investigated using the Single Parabolic Band (SPB) model both when Br doping increased the fraction of the hexagonal phase ($SnSe_{2-x}Br_x$ for $x < 0.05$) and when it only increased the n_H as the $SnSe_{2-x}Br_x$ was fully hexagonal ($x \geq 0.05$). The increase of the hexagonal phase improved the PF of the $SnSe_{2-x}Br_x$ ($x < 0.05$) due to a significant increase in the non-degenerate mobility (μ_0). The increase in the Br doping concentration (x) for $x > 0.05$ also improved the PF but this time by increasing the density-of-states effective mass (m_d^*). The theoretical maximum PF of 1.27 mW m^{-1} K^{-2} was predicted when $x = 0.03$ (when the $SnSe_{2-x}Br_x$ is not yet in full hexagonal phase) at room temperature. An additional 12% increase in 300 K zT (0.21 → 0.23) of $SnSe_{1.7}Br_{0.3}$ ($x = 0.03$) was expected once the n_H was optimally tuned as the SPB model guided. Understanding the effects of Br doping on the electronic band structure of $SnSe_2$, which changes with doping concentration, would enable the development of $SnSe_2$ materials with tailored thermoelectric properties.

Single parabolic band model calculation

Electronic band parameters such as m_d^*, μ_0, weighted mobility (μ_W), and B-factor were calculated using the SPB model while assuming that only one parabolic band contributed to the electronic transport properties and that the acoustic phonon scattering mechanism was the dominant charge scattering mechanism. The purpose of employing the SPB model here is to guide the improvement of zT. Because most of the parameters in zT vary with n_H, the optimization of the n_H is essential for the zT increase. While the vast compositional space of promising thermoelectric materials offers immense potential, efficient optimization transcends solely experimental methods. While computationally intensive methods exist, for experimentalists, simplified Boltzmann transport equation-derived models often provide a pragmatic route to understand thermoelectric material properties. The SPB model, relying on a single parabolic band and effective mass, stands out for its simplicity and effectiveness. Notably, it enables complete characterization of the system using a minimal set of experimentally obtainable quantities (S, σ, κ, and n_H), demonstrating its practical utility and simplicity.

Estimation of density-of-states effective mass, m_d^*

Based on the experimental temperature-dependent S and 300 K n_H from Liu *et al.*,[26] n_H-dependent S at 300 K was obtained. The m_d^* corresponding to the 300 K n_H-dependent S measurement was then acquired by fitting the theoretical n_H-dependent S constructed from the following eqn (2)–(4) to the n_H-dependent S measurement.

$$S = \frac{k_B}{e}\left(\eta - \frac{2F_1(\eta)}{F_0(\eta)}\right) \quad (2)$$

$$F_j(\eta) = \int_0^\infty \frac{\varepsilon^j}{1+\exp(\varepsilon-\eta)}\mathrm{d}\varepsilon \quad (3)$$

$$n_H = \frac{16\pi}{3}\left(\frac{2m_d^* k_B T}{h^2}\right)^{3/2}\frac{(F_0(\eta))^2}{F_{-0.5}(\eta)} \quad (4)$$

where k_B, e, η, F_j, and h are the Boltzmann constant, electron charge, reduced chemical potential, fermi integral order of j, and Planck's constant, respectively. According to eqn (2)–(4) while the S is only a function of η, the n_H varies with both η and m_d^*. We changed η from −20 to 20 with a fitted m_d^* to calculate a theoretical Seebeck pisarenko curve (S *vs.* n_H) that agreed with the experimental n_H-dependent S.[26]

Estimation of non-degenerate mobility, μ_0

We computed theoretical n_H-dependent Hall mobility (μ_H) using eqn (4) and (5).[27]

$$\mu_H = \mu_0 \frac{F_{-0.5}(\eta)}{2F_0(\eta)} \quad (5)$$

The μ_0 included in μ_H (eqn (5)) was fitted so that the theoretical n_H-dependent μ_H agreed with the experimental n_H-dependent μ_H. When the n_H was calculated to construct the theoretical n_H-dependent μ_H, the same m_d^* fitted to construct the n_H-dependent S of the same sample was adopted.

Estimation of weighted mobility, μ_W, and B-factor, B

Once we have obtained the m_d^* and μ_0 of the $SnSe_{2-x}Br_x$ samples, corresponding μ_W and B-factor were calculated using the following eqn (6) and (7), respectively.[32–34] In eqn (6) and (7), the m_e is the electron rest mass.

$$\mu_w = \mu_0 \left(\frac{m_d^*}{m_e}\right)^{3/2} \quad (6)$$

$$B = \left(\frac{k_B}{e}\right)^2 \frac{8\pi e (2 m_e k_B)^{3/2}}{h^3} \frac{\mu_w T^{5/2}}{\kappa_l} \quad (7)$$

Results and discussion

Fig. 1(a) shows the experimental and calculated n_H-dependent S of $SnSe_{2-x}Br_x$ samples ($x = 0$, 0.01, 0.03, 0.05, 0.1) at 300 K. The symbols represent those measurements reported by Liu *et al.*[26]

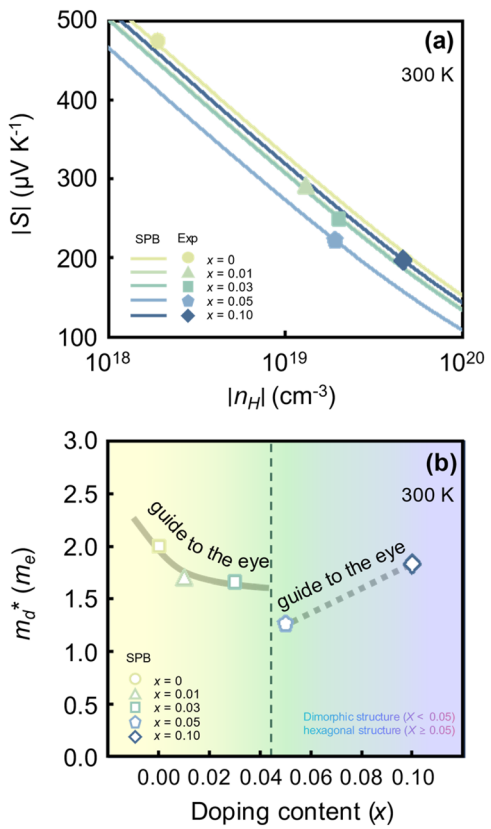

Fig. 1 (a) Experimental (symbols) and theoretical (lines) Hall carrier concentration (n_H)-dependent Seebeck coefficient (S) of $SnSe_{2-x}Br_x$ (x = 0–0.10) at 300 K.[26] (b) Density-of-states effective mass (m_d^*) as a function of Br doping content (x) at 300 K.

(refer to Fig. S1(a) in ESI† for temperature-dependent S of $SnSe_{2-x}Br_x$ at higher temperatures). The lines represent theoretical S as a function of n_H for different x computed by using the SPB model. The experimental S (in symbols) decreases as x increases. The rate of S decrease is particularly high when x is low. For example, the experimental S of pristine $SnSe_2$ ($x = 0$) decreases by more than 39% when x increases to 0.01 (475 → 289 μV K^{-1}). In contrast, the experimental n_H generally increases as x increases. For example, the n_H of the $x = 0.1$ sample (4.6×10^{19} cm^{-3}) is higher than that of the pristine sample (0.19×10^{19} cm^{-3}) by more than a factor of 24. However, when x increases from 0.03 to 0.05, we observe a slight drop in n_H from 2.0×10^{19} to 1.9×10^{19} cm^{-3}. The x increase increases the fraction of the hexagonal phase within the sample only for $x < 0.05$. Because the $SnSe_{2-x}Br_x$ samples with $x \geq 0.05$ is fully hexagonal, the effect of Br doping would be different from that observed at $x < 0.05$. It is when the sample becomes fully hexagonal ($x = 0.05$) that we observe an exception in the general trend of increasing n_H with an increasing x. The calculated n_H-dependent S obtained by fitting m_d^* (in lines) are all in agreement with the symbol data. This implies that the fitted m_d^* accurately reflects the electronic band structure of the $SnSe_{2-x}Br_x$ samples.

Fig. 1(b) shows the x-dependent m_d^* fitted using the SPB model at 300 K. Fig. 1(b) is divided into two regions: yellow and purple regions. The yellow region is when the $SnSe_{2-x}Br_x$ samples exist as a dimorphic phase (hexagonal structure + unidentified structure). As the x increases from 0 to 0.05, the fraction of the hexagonal phase increases. At $x = 0.05$, the $SnSe_{2-x}Br_x$ becomes fully hexagonal. The color of the background also changes from yellow to purple at $x = 0.05$, which means that the dimorphic structure transforms to the full hexagonal structure. For $x \geq 0.05$, the samples are all hexagonal. So this region is colored in purple. The m_d^* decreases from the pristine sample to $x = 0.05$ sample. For example, the m_d^* of pristine and $x = 0.05$ sample are 2.00 m_e and 1.26 m_e, respectively. This 37% decrease in m_d^* is closely related to the dimorphic structure changing to fully hexagonal phase. Once the Br doping finishes stabilizing the hexagonal phase, further Br doping starts to increase the m_d^* again. The m_d^* of the $x = 0.1$ sample increase to 1.83 m_e, which is approximately 45% heavier than that of $x = 0.05$ sample. The m_d^* increase at $x > 0.05$ may be related to the band convergence. According to Kim *et al.*,[34] there exists another conduction band near (in energy) the major conduction band in the calculated band structure of $SnSe_2$. However, the change in μ_0 with increasing x also needs to be evaluated to confirm a possible band convergence at $x > 0.5$. Our m_d^* for $SnSe_{2-x}Br_x$ determined by the SPB model spans a range of ~1.0 to 2.0 m_e, aligning with values reported in previous studies also using the SPB model.[35]

Fig. 2(a) shows the experimental and calculated n_H-dependent μ_H at 300 K. The symbols represent the experimental n_H-dependent μ_H of $SnSe_{2-x}Br_x$ ($x = 0$, 0.01, 0.03, 0.05, 0.1) at 300 K reported by Liu *et al.*[26] (refer to Fig. S1(b)† for temperature-dependent σ of $SnSe_{2-x}Br_x$ at higher temperatures). The lines represent the n_H-dependent μ_H calculated using the SPB model. The experimental μ_H initially increases as the x increases from

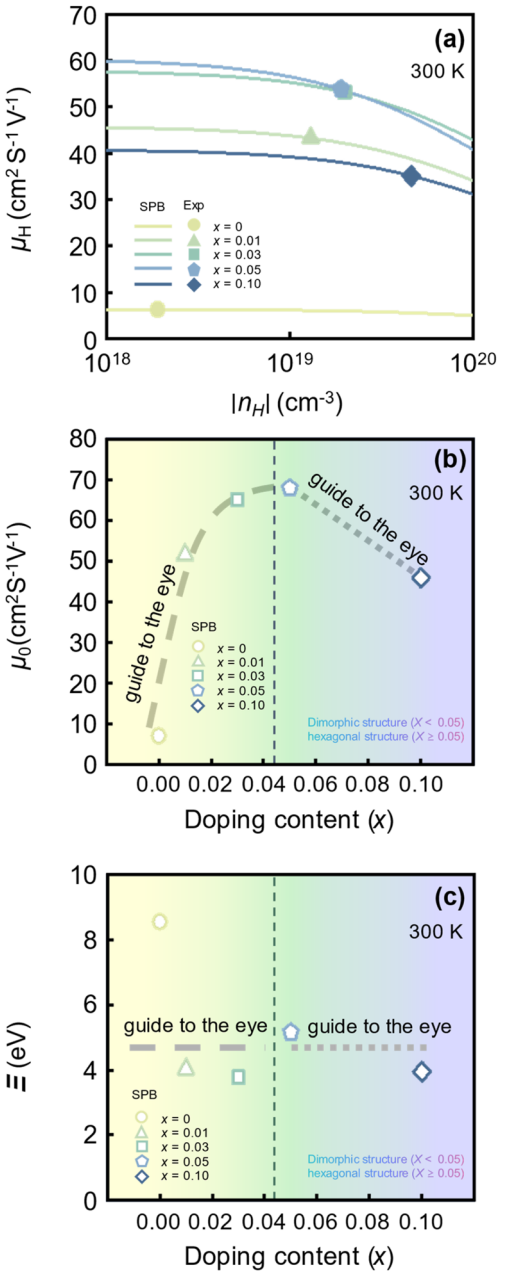

Fig. 2 (a) Experimental (symbols) and theoretical (lines) Hall carrier concentration (n_H)-dependent hall mobility (μ_H) of $SnSe_{2-x}Br_x$ ($x = 0$–0.1) at 300 K.[26] (b) Non-degenerate mobility (μ_0) and (c) deformation potential (Ξ) as a function of Be doping content (x) at 300 K.

0 to 0.03. The amount of μ_H increase rapidly decreases as x approaches 0.03. When the x increases from 0.03 to 0.05, the change in μ_H is almost negligible. However, as x further increases to 0.1, the corresponding μ_H decreases significantly. The μ_H of the $x = 0.05$ sample (53.9 $cm^2\ V^{-1}\ s^{-1}$) is approximately 8 times higher than that of the pristine sample (6.3 $cm^2\ V^{-1}\ s^{-1}$). However, the μ_H of the $x = 0.1$ sample is 35% lower than that of the $x = 0.05$ sample. As the fraction of hexagonal structures occupying dimorphic structures increases up to $x = 0.05$, the corresponding μ_H increases. However, once the hexagonal structure is stabilized Br doping decreases the μ_H.

Fig. 2(b) shows the x-dependent μ_0 calculated using the SPB model. The μ_0 as a function of x resembles an inverted U-shape. As the fraction of the hexagonal phase increases the μ_0 saturates to 68.0 $cm^2\ V^{-1}\ s^{-1}$ at $x = 0.05$. It is to be noted that the slight increase in hexagonal phase fraction significantly improves the μ_0. For $x \geq 0.05$, as the Br doping content increases in the fully hexagonal $SnSe_{2-x}Br_x$ samples, the μ_0 rapidly decreases back to 46.0 $cm^2\ V^{-1}\ s^{-1}$ ($x = 0.1$). This is exactly the opposite of the trend observed in x-dependent m_d^* (Fig. 1(b)). If the change in μ_0 with an increasing x for $x \geq 0.05$ is negligible, we could have concluded that the m_d^* increase for $x \geq 0.05$ is due to band convergence. On the contrary, the m_d^* increase accompanied by a decrease in μ_0 can be characterized by a simple band flattening which is not beneficial to the PF improvement. However, while the majority band is being flattened, the neighbouring band may also contribute to the electronic transport due to Br doping. This can be evaluated when the weighted mobility (μ_W) is calculated.

Fig. 2(c) shows the x-dependent deformation potential (Ξ) calculated by the SPB model. The Ξ is closely related to the μ_0 as defined in eqn (8).

$$\mu_0 = \left(\frac{e\pi\hbar^4 C_l}{\sqrt{2}\Xi^2 (k_B T)^{3/2}}\right)\left(\frac{1}{m_b^*}\right)^{5/2} \quad (8)$$

where the C_l and m_b^* are the elastic constant and the single band mass, respectively. The m_b^* is coupled to m_d^* as shown below.

$$m_d^* = N_V^{2/3} m_b^* \quad (9)$$

The product between $N_V^{2/3}$ and m_b^*, where N_V is the valley degeneracy, defines the m_d^*. When the m_d^* increase is driven by the N_V increase (no change in m_b^*), the band convergence occurs.[13,28] However, when m_d^* increase is driven by the m_b^* increase (no change in N_V), a band flattening occurs. For this reason, the nature of m_d^* increase needs to be evaluated by the corresponding change in μ_0. Unlike μ_0, the Ξ is independent of m_d^* and captures the strength of the carrier–phonon interaction. According to Fig. 2(c), Br doping in $SnSe_2$ decreases the Ξ, but varying Br doping content (x) does not have a strong impact on the Ξ. For example, the Ξ of SnTe decreased by more than 55% when it is doped with $x = 0.01$ Br (8.56 → 3.79 eV). However, it remained relatively constant for increasing x. In other words, neither changing the hexagonal phase ($x < 0.05$) nor increasing the Br doping content in a stabilized hexagonal phase ($x \geq 0.05$) has a significant impact on how phonons scatter charged carriers.

Fig. 3(a) shows the x-dependent μ_W of $SnSe_{2-x}Br_x$ ($x = 0.0$–0.10) calculated by using the SPB model at 300 K. The μ_W, which is defined as the product of μ_0 and $(m_d^*/m_e)^{3/2}$ (as presented in eqn (6)), captures the potential of a material achieve a high PF, as it depends on both the μ_0 and the m_d^*. Compared to the pristine $SnSe_2$ sample ($x = 0.0$), the Br-doped $SnSe_2$ samples ($x > 0.0$) have a significantly higher μ_W. When Br doping increases the fraction of the hexagonal phase ($x < 0.05$), the μ_W increases

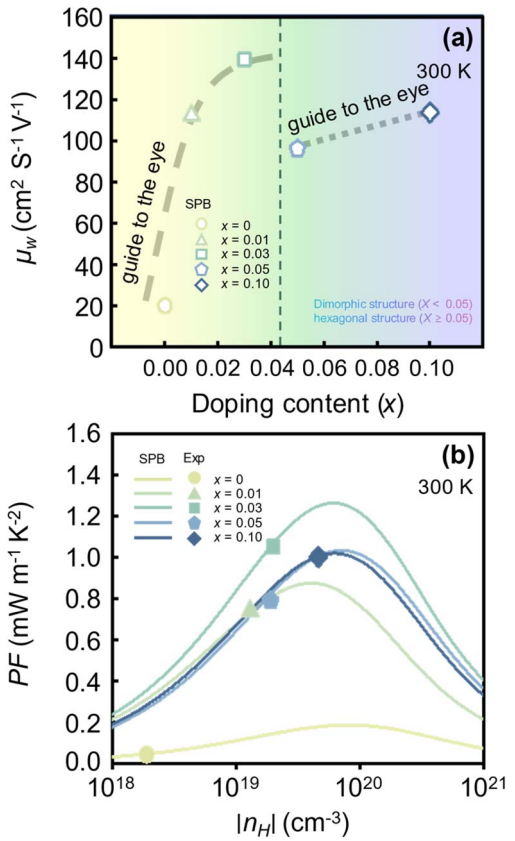

Fig. 3 (a) Calculated weighted mobility (μ_W) of $SnSe_{2-x}Br_x$ (x = 0.0–0.10) estimated with varying Br doping content (x) at 300 K. (b) Calculated and experimental Hall carrier concentration (n_H)-dependent power factor (PF) of $SnSe_{2-x}Br_x$ (x = 0.0–0.10) at 300 K.[26]

significantly (guide-to-the-eye in grey line). For example, the μ_W of the pristine sample (x = 0.0) and the x = 0.03 sample are 20.22 and 139.39 cm^2 V^{-1} s^{-1}, respectively, which is a 5.8-fold increase. Additional Br doping on stabilized hexagonal phase ($x \geq 0.05$) also improves the μ_W (guide-to-the-eye in grey line). Although the μ_W increase is observed for both $x < 0.05$ and $x \geq 0.05$ regions with increasing x, the reason behind the μ_W improvement differs. When $x < 0.05$, the μ_W increase with x is due to the μ_0 increase (Fig. 2(b)), but when $x \geq 0.05$, the μ_W increase can be attributed to the m_d^* increase (Fig. 1(b)). The increase in m_d^* with increasing x at $x \geq 0.05$ is due to both band flattening and band convergence. Specifically, the lowest conduction band that contributes majorly to electronic transports becomes heavier, while the second lowest conduction band approaches the lowest conduction band in energy as Br is doped into the fully hexagonal $SnSe_2$. Evidence for band flattening and band convergence is provided by the decrease in μ_0 (Fig. 2(b)) and the increase in μ_W (Fig. 3(a)) at $x \geq 0.05$, respectively. The discontinuity in the μ_W when x increases from 0.03 to 0.05 is due to a sudden drop in the m_d^* of the fully hexagonal phase x = 0.05 sample (Fig. 1(b)). Although the unidentified phase comprises a small fraction of the x = 0.03 sample, its conversion to hexagonal phase is responsible for the decrease in m_d^*.

Fig. 3(b) shows the PF as a function of the n_H. The experimentally measured PF reported by Liu *et al.*[26] is represented by the symbols, while the theoretically calculated PF is represented by the lines. Experimentally, Br doping improves the PF in both $x < 0.05$ and $x \geq 0.05$ regions. When $x < 0.05$, the PF of the x = 0.03 sample (1.05 mW m^{-1} K^{-2}) is approximately 25 times higher than that of the pristine SnS_2 sample (0.04 mW m^{-1} K^{-2}). For $x \geq 0.05$, the PF of the x = 0.10 sample (1.00 mW m^{-1} K^{-2}) is 27% higher than that of the x = 0.05 sample (0.79 mW m^{-1} K^{-2}). From the x-dependent μ_W (Fig. 3(a)), we found that both band flattening and band convergence are present in the x = 0.10 sample. However, the theoretical maximum PF of the x = 0.10 sample (1.02 mW m^{-1} K^{-2}) is not as high as that of the x = 0.03 sample (1.27 mW m^{-1} K^{-2}). According to the SPB model, the PF of the x = 0.03 sample can be enhanced by more than 21% with an appropriate optimization of the n_H (1.05 → 1.27 mW m^{-1} K^{-2}). The theoretical maximum PF and its corresponding n_H predicted by the SPB model exhibit reasonable agreement with those obtained from Density Functional Theory (DFT) calculations. For example, the SPB model predicts a peak PF of 0.17 mW m^{-1} K^{-2} for pristine $SnSe_2$ (x = 0) at $n_H = 8 \times 10^{19}$ cm^{-3} (Fig. 3(b)), while DFT calculations yield a peak PF of 0.13 mW m^{-1} K^{-2} at $n = 5 \times 10^{19}$ cm^{-3}.[36] It is important to note that the maximum PF is predicted to occur before the sample is fully hexagonal.

Fig. 4(a) shows the x-dependent B-factor of $SnSe_{2-x}Br_x$ (x = 0.0–0.10) at 300 K calculated by the SPB model. The B-factor, which is proportional to the ratio of μ_0 to κ_l, is related to the theoretically achievable zT (eqn (7)). The trend observed in the B-factor is similar to that observed in the μ_0, as shown in Fig. 3(a). This is possible because the κ_l of the Br-doped $SnSe_2$ decreases linearly with increasing x (Fig. 4(b)). When Br was first doped into $SnSe_2$ with x = 0.01, its κ_l increased by 11% compared to the pristine $SnSe_2$ (1.34 → 1.48 W m^{-1} K^{-1}). However, when x was increased further, the κ_l decreased gradually. Both increasing the hexagonal phase fraction ($0 < x < 0.05$) and increasing the Br doping in the full hexagonal phase ($x \geq 0.05$) reduced the κ_l (refer to Fig. S1(c)† for temperature-dependent total thermal conductivity (κ_{tot}) of $SnSe_{2-x}Br_x$ at higher temperatures). The calculated Lorenz number (L) and κ_e used to estimate κ_l are provided in Fig. S2.† Initial increase in the κ_l of the x = 0.01 sample requires further study. While an initial increase in κ_l upon Br doping of $SnSe_2$ has been reported previously,[37] similar observations in Cl-doped $SnSe_2$ suggest a broader phenomenon beyond specific dopant species.[38] Elucidating the underlying mechanism governing this low-concentration dopant-induced thermal conductivity enhancement warrants further investigation. The effect of decreasing the unidentified phase on the B-factor is stronger than that of increasing the Br doping content in the fully hexagonal phase. Although the B-factor improved by a factor of 6 when pristine $SnSe_2$ was doped with x = 0.03 (0.01 → 0.06), once $SnSe_2$ was fully hexagonal, additional Br doping only improved the B-factor by 25% as x increased from 0.05 to 0.10 (0.04 → 0.05). However, if the x is increased beyond 0.10, the B-factor of the sample may become higher than that of the x = 0.03 sample due

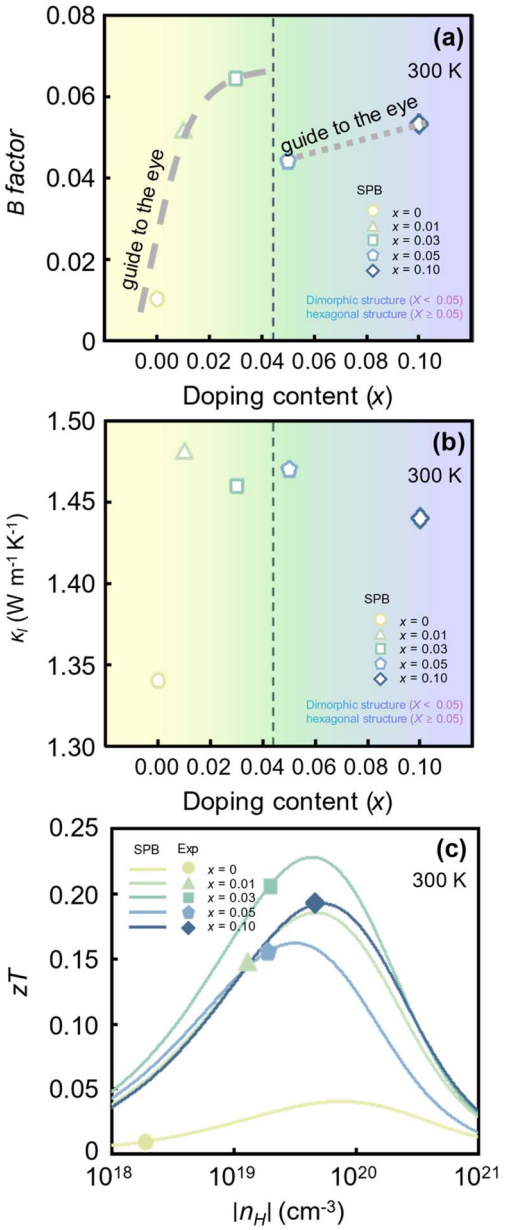

Fig. 4 Calculated (a) B-factor and (b) lattice thermal conductivity (κ_l) of $SnSe_{2-x}Br_x$ (x = 0.0–0.10) at 300 K. (c) Calculated and experimental[27] zT of $SnSe_{2-x}Br_x$ (x = 0.0–0.10) with varying Hall carrier concentration (n_H).

to the combined effects of band convergence and κ_l reduction becoming stronger.

Fig. 4(c) shows experimental and calculated n_H-dependent zT at 300 K (refer to Fig. S1(d)† for temperature-dependent zT of $SnSe_{2-x}Br_x$ at higher temperatures). The symbols represent the measured values.[26] The lines represent zT computed by the SPB model-based calculation. The calculated maximum zT of pristine $SnSe_2$ is low, as illustrated in Fig. 4(c). Temperature-dependent zT calculations for pristine $SnSe_2$ below 300 K are presented in Fig. S1 (ESI†), revealing a maximum at 300 K exceeding those at 50 and 100 K. This finding underscores the pronounced temperature-dependent zT of $SnSe_2$.[24] However, the maximum zT improves drastically as Br is doped into $SnSe_2$. For example, the calculated maximum zT of pristine $SnSe_2$ and x = 0.03 samples are 0.04 and 0.23, respectively, which is an increase of more than 5 times. Once the $SnSe_2$ is a fully hexagonal phase ($x \geq 0.05$), additional Br doping is also beneficial to the calculated maximum zT. The calculated maximum zT of the x = 0.05 and 0.10 samples are 0.16 and 0.19, respectively (19% improvement in zT). According to the SPB model calculations, adjusting the n_H of the x = 0.03 sample to 3.6 × 10^{19} cm^{-3} can improve the zT to 0.23, an approximately 10% increase compared to the experimental zT. Furthermore, it is highly likely that further Br doping beyond x = 0.10 may result in even higher zT because of the interplay between the band convergence and intensified point-defect phonon scattering.

Conclusions

In summary, the effect of Br doping on the electronic band structure of dimorphic $SnSe_2$ ($SnSe_{2-x}Br_x$ for x = 0, 0.01, 0.03, 0.05, and 0.10) is investigated using the Single Parabolic Band (SPB) model. For Br doping concentrations (x) < 0.05, the fraction of the majority hexagonal phase increases with x, while the other phase remains unidentified. On the contrary, for $x \geq 0.05$, the Br-doped $SnSe_2$ is fully hexagonal. For all x, the Hall carrier concentration (n_H) increases with x. The mechanisms underlying the power factor improvement of Br-doped $SnSe_2$ with increasing n_H differ depending on the x. For x < 0.05, the increasing hexagonal phase significantly improves the mobility, while for the $x \geq 0.05$, the power factor is improved by a combination of band convergence and band flattening. The highest power factor is predicted when a small amount of unidentified phase exists in the $SnSe_{2-x}Br_x$ (x = 0.03). Characterization of the unidentified phase in the dimorphic $SnSe_2$ is to be carried out to tailor the thermoelectric properties of the $SnSe_2$.

Author contributions

Se-Jun Kim: conceptualization, investigation, writing – original draft. Minsu Heo: investigation, software, writing – original Draft. Sang-il Kim: validation, methodology, writing – original draft. Hyunjin Park: data curation. Jeong-Yeon Kim: visualization. Won-Seon Seo: validation. Hyun-Sik Kim: supervision, funding acquisition, writing – review & editing.

Conflicts of interest

There are no conflicts to declare.

Acknowledgements

This work was supported by the National Research Foundation of Korea (NRF) grant funded by the Korea government (MSIT) (RS-2023-00212959). This research was also supported by Basic Science Research Program through the National Research Foundation of Korea (NRF) funded by the Ministry of Education (NRF-2019R1A6A1A11055660).

Notes and references

1 T. Wu, L. Xia, M. Zhuang, J. Pan, J. Liu, W. Dai, Z. Zhao, M. Zhang, X. Shen, P. He, J. Zhang and Y. Qin, *J. Mar. Sci. Eng.*, 2023, **11**, 9.
2 O. Adam, N. Liberty-Levi, M. Byrne and T. Birner, *Geophys. Res. Lett.*, 2022, **50**, e2022GL102546.
3 A. A. Khasnis and M. D. Nettleman, *Arch. Med. Res.*, 2005, **36**, 689–696.
4 J. Lee, K. A. Lin, S. Jung and E. E. Kwon, *Chem. Eng. J.*, 2023, **452**, 139218.
5 S. LeBlanc, *Sustainable Mater. Technol.*, 2014, **1–2**, 26–35.
6 P. Fernández-Yáñez, V. Romero, O. Armas and G. Cerretti, *Appl. Therm. Eng.*, 2021, **196**, 117291.
7 Y. Zheng, Q. Zhang, X. Su, H. Xie, S. Shu, T. Chen, G. Tan, Y. Yan, X. Tang, C. Uher and G. J. Snyder, *Adv. Energy Mater.*, 2014, **5**, 1401391.
8 A. Pham, T. Vu, C. Cheng, T. Trinh, J.-E. Lee, H. Ryu, C. Hwang, S.-K. Mo, J. Kim, L. Zhao, A. Duong and S. Cho, *ACS Appl. Energy Mater.*, 2020, **3**, 10787–10792.
9 D. Enescu and E. O. Virjoghe, *Renew. Sust. Energ. Rev.*, 2014, **38**, 903–916.
10 C. Zhou, Y. K. Lee, Y. Yu, S. Byun, Z.-Z. Luo, H. Lee, B. Ge, Y.-L. Lee, X. Chen, J. Y. Lee, O. Cojocaru-Mirédin, H. Chang, J. Im, S.-P. Cho, M. Wuttig, V. P. Dravid, M. G. Kanatzidis and I. Chung, *Nat. Mater.*, 2021, **20**, 1378–1384.
11 A. Sakai, T. Kanno, K. Takahashi, H. Tamaki, H. Kusada, Y. Yamada and H. Abe, *Sci. Rep.*, 2014, **4**, 6089.
12 Y. Pei, H. Wang and G. J. Snyder, *Adv. Mater.*, 2012, **24**, 6125–6135.
13 K. H. Lee, S.-i. Kim, H.-S. Kim and S. W. Kim, *ACS Appl. Energy Mater.*, 2020, **3**, 2214–2223.
14 S. Ning, S. Huang, Z. Zhang, N. Qi, M. Jiang, Z. Chen and X. Tang, *J. Materiomics*, 2022, **8**, 1086–1094.
15 M. Heo, S.-H. Kwon, S.-i. Kim, H. Park, K. H. Lee and H.-S. Kim, *J. Alloys Compd.*, 2023, **954**, 170144.
16 Y. Zheng, T. J. Slade, L. Hu, X. Y. Tan, Y. Luo, Z.-Z. Luo, J. Xu, Q. Yan and M. G. Kanatzidis, *Chem. Soc. Rev.*, 2021, **50**, 9022–9054.
17 V. Karthikeyan, S. L. Oo, J. U. Surjadi, X. Li, V. C. S. Theja, V. Kannan, S. C. Lau, Y. Lu, K. Lam and V. A. L. Roy, *ACS Appl. Mater. Interfaces*, 2021, **13**, 58701–58711.
18 Y. Zhang, Z. Li, S. Singh, A. Nozariasbmarz, W. Li, A. Genç, Y. Xia, L. Zheng, S. H. Lee, S. K. Karan, G. K. Goyal, N. Liu, S. M. Mohan, Z. Mao, A. Cabot, C. Wolverton, B. Poudel and S. Priya, *Adv. Mater.*, 2022, **35**, 2208994.
19 Y. Wu, W. Li, A. Faghaninia, Z. Chen, J. Li, X. Zhang, B. Gao, S. Lin, B. Zhou, A. Jain and Y. Pei, *Mater. Today Phys.*, 2017, **3**, 127–136.
20 G. Li, G. Ding and G. Gao, *J. Condens. Matter Phys.*, 2016, **29**, 015001.
21 S. Bai, M. Wu, J. Zhang, D. Luo, D. Wan, X. Li and S. Tang, *Chem. Eng. J.*, 2023, **455**, 140832.
22 C. Zhou, Y. Yu, X. Zhang, Y. Cheng, J. Xu, Y. K. Lee, B. Yoo, O. Cojocaru-Mirédin, G. Liu, S.-P. Cho, M. Wuttig, T. Hyeon and I. Chung, *Adv. Funct. Mater.*, 2019, **30**, 1908405.
23 S. Wu, C. Liu, Z. Wu, L. Miao, J. Gao, X. Hu, J. Chen, Y. Zheng, X. Wang, C. Shen, H. Yang and X. Zhou, *Ceram. Int.*, 2019, **45**, 82–89.
24 J. Wang, X. Jia, S. Lou, G. Li and S. Zhou, *ACS Omega*, 2020, **5**, 12409.
25 F. Li, Z. Zheng, W. Wang, J.-F. Li, B. Li, A. Zhong, J. Luo and P. Fan, *J. Mater. Sci.*, 2017, **52**, 10506–10516.
26 M. Liu, J. Zhang, J. Xu, B. Hu, B. Liu, K. Sun, Y. Yang, J. Wang and B. Du, *J. Solid State Chem.*, 2020, **289**, 121468.
27 H. Park, S.-i. Kim, J.-Y. Kim, S.-M. Hwang and H.-S. Kim, *Ceramics*, 2023, **6**, 504–513.
28 H.-S. Kim, N. A. Heinz, Z. M. Gibbs, Y. Tang, S. D. Kang and G. J. Snyder, *Mater. Today*, 2017, **20**, 452–459.
29 V. P. Bhatt, K. Gireesan and G. R. Pandya, *J. Cryst. Growth*, 1989, **96**, 649–651.
30 L. Amalraj, M. Jayachandran and C. Sanjeeviraja, *Mater. Res. Bull.*, 2004, **39**, 2193–2201.
31 M. Kumar, S. Rani, Y. Singh, K. S. Gour and V. N. Singh, *RSC Adv.*, 2021, **11**, 6477–6503.
32 H. Naithani and T. Dasqupta, *ACS Appl. Energy Mater.*, 2020, **3**, 2200–2213.
33 M. Kim, S.-i. Kim, S. W. Kim, H.-S. Kim and K. H. Lee, *Adv. Mater.*, 2021, **33**, 2005931.
34 S.-i. Kim, J. Bang, J. An, S. Hong, G. Bang, W. H. Shin, T. Kim and K. Lee, *J. Alloys Compd.*, 2021, **868**, 159161.
35 Y. Wu, W. Li, A. Faghaninia, Z. Chen, J. Li, X. Zhang, B. Gao, S. Lin, B. Zhou, A. Jain and Y. Pei, *Mater. Today*, 2017, **3**, 127–136.
36 D. Sree Sourav, Md. Golam Rosul and M. Zebarjadi, *J. Phys. Chem. C*, 2017, **127**, 6916–6924.
37 C. Zhou, Y. Yu, X. Zhang, Y. Cheng, J. Xu, Y. K. Lee, B. Yoo, O. Cojocaru-Mirédin, G. Liu, S.-P. Cho, M. Wuttig, T. Hyeon and I. Chung, *Adv. Funct. Mater.*, 2020, **30**, 1908405.
38 S. Wu, C. Liu, Z. Wu, L. Miao, J. Gao, X. Hu, J. Chen, Y. Zheng, X. Wang, C. Shen, H. Yang and X. Zhou, *Ceram. Int.*, 2019, **45**, 82.